Journal of
Functional Biomaterials

MDPI

Article

Strength–Ductility Synergy in Biodegradable Mg-Rare Earth Alloy Processed via Multi-Directional Forging

Faseeulla Khan Mohammad [1,†], Uzwalkiran Rokkala [2,*,†], Sohail M. A. K. Mohammed [3,*], Hussain Altammar [1], Syed Quadir Moinuddin [1] and Raffi Mohammed [4]

[1] Department of Mechanical Engineering, College of Engineering, King Faisal University, Al-Ahsa 31982, Saudi Arabia
[2] Department of Mechanical Engineering, Aditya University, Surampalem 533437, India
[3] Department of Aerospace and Mechanical Engineering, The University of Texas at El Paso, El Paso, TX 79968, USA
[4] Department of Metallurgical and Materials Engineering, National Institute of Technology Andhra Pradesh, Tadepalligudem 534101, India
* Correspondence: uzwalkiranr@adityauniversity.in (U.R.); smmohammed@utep.edu (S.M.A.K.M.)
† These authors contributed equally to this work.

Abstract

In this study, a biodegradable Mg-Zn-Nd-Gd alloy was processed via multi-directional forging (MDF) to evaluate its microstructural evolution, mechanical performance, and corrosion behavior. Electron backscattered diffraction (EBSD) analysis was conducted to evaluate the influence of grain size and texture on mechanical strength and corrosion resistance. The average grain size decreased significantly from 118 ± 5 μm in the homogenized state to 30 ± 10 μm after six MDF passes, primarily driven by discontinuous dynamic recrystallization (DDRX). Remarkably, this magnesium (Mg) alloy exhibited a rare synergistic enhancement in both strength and ductility, with ultimate tensile strength (UTS) increasing by ~59%, yield strength (YS) by ~90%, while elongation improved by ~44% unlike conventional severe plastic deformation (SPD) techniques that often sacrifice ductility for strength. This improvement is attributed to grain refinement, dispersion strengthening from finely distributed $Mg_{12}Nd$ and Mg_7Zn_3 precipitates, and texture weakening, which facilitated the activation of non-basal slip systems. Despite the mechanical improvements, electrochemical corrosion testing in Hank's balanced salt solution (HBSS) at 37 °C revealed an increased corrosion rate from 0.1165 mm/yr in homogenized condition to 0.2499 mm/yr (after six passes of MDF. This was due to the higher fraction of low-angle grain boundaries (LAGBs), weak basal texture, and the presence of electrochemically active fine Mg_7Zn_3 particles. However, the corrosion rate remained within the acceptable range for bioresorbable implant applications, indicating a favorable trade-off between mechanical performance and degradation behavior. These findings demonstrate that MDF processing effectively enhances the strength–ductility synergy of Mg-rare earth alloys while maintaining a clinically acceptable degradation rate, thereby presenting a promising route for next-generation biomedical implants.

Keywords: Mg-Zn-Nd-Gd alloy; multi-directional forging; grain refinement; mechanical properties; corrosion and bioimplants

check for updates

Academic Editors: Dapeng Zhao, Hong Wu and Jing Bai

Received: 18 September 2025
Revised: 11 October 2025
Accepted: 15 October 2025
Published: 18 October 2025

Citation: Mohammad, F.K.; Rokkala, U.; Mohammed, S.M.A.K.; Altammar, H.; Moinuddin, S.Q.; Mohammed, R. Strength–Ductility Synergy in Biodegradable Mg-Rare Earth Alloy Processed via Multi-Directional Forging. *J. Funct. Biomater.* **2025**, *16*, 391. https://doi.org/10.3390/jfb16100391

Copyright: © 2025 by the authors. Licensee MDPI, Basel, Switzerland. This article is an open access article distributed under the terms and conditions of the Creative Commons Attribution (CC BY) license (https://creativecommons.org/licenses/by/4.0/).

1. Introduction

Biodegradable implants are the new generation implants, gaining more attention due to their degradable properties without a nontoxic nature [1,2]. The major advantages of

biodegradable implants are to avoid secondary surgeries, thus patients feel comfort and a reduction in hospital stay costs [3]. For a few decades, polymer-based biodegradable implants have been used for surgeries and implantations [4]. However, the primary problem with polymer-based composites fail due to their lower strength and bacterial infections. Therefore, researchers are looking for metal-based degradable implants that possess high, acceptable strength and good biological properties. The major metal degradable materials are Mg- and Iron (Fe)-based alloys [5]. However, Mg and its alloys are widely used as biodegradable metal implants due to their unique properties, such as biocompatibility and a Young's modulus similar to natural bone, which make them more suitable than Fe-based alloys [6,7]. Various Mg-based alloys, such as Mg-Ca, Mg-Al, Mg-Zn, and Mg-rare earth element alloys, are being developed to produce high-quality metal biodegradable implants [8]. Alloys such as Mg-Y, WE43, etc., are the recent wrought alloys used in real-time clinical applications [9,10]. However, some challenges are associated with the currently available commercial Mg-based implants. One of the major limitations is low strength and early degradation [11,12].

Recent studies are focused on developing Mg-based biodegradable implants with sufficient strength, controlled degradation rates, and excellent biocompatibility. Several methods such as alloying [13–15], composites [16–18], modifying the microstructure using SPD techniques such as equal channel angular pressing [19], MDF or multi axial forging (MAF) [20], friction stir processing [21], high pressure torsion, accumulative roll bonding [22], and cyclic extrusion and compression [23] are used. Out of these processes, MDF/MAF has been adopted for processing Mg materials at different processing conditions (strain and temperature). Further, this process is found to be the most promising and unique for miniature applications such as biomedical devices, which require both high strength and acceptable corrosion resistance [24,25]. Anne et al. [26] characterized the Mg-4Zn alloy processed at 280 °C up to five passes. The results reported that the corrosion properties increased with increasing number of MDF passes. This was attributed to the grain refinement and thus an increase in length/area of grain boundaries, which acted as a physical barrier. The samples processed at five passes exhibited a very fine grain structure, and mechanical properties of the alloy increased up to three passes and reduced further, which was a result of strain hardening and inverse Hall-Petch mechanism [26]. Similar results were observed by Ramesh et al. [27] when an Mg-6Zn alloy was processed up to five passes and obtained a minimum grain size of 5 μm, possessing a large number of dislocations and high-angle grain boundaries (HAGBs). There was a significant improvement in the tensile properties and corrosion resistance up to five passes, which was attributed to the grain refinement, high dislocation densities, and strain hardening.

Similarly, Cao et al. conducted MDF of Mg-4Zn-2Gd-0.5Ca alloy at 350 °C. They observed that the corrosion resistance of the alloy varied under different processing conditions, which they attributed to the presence of second-phase particles, specifically Mg_3Zn_6Gd and $Mg_3Zn_3Gd_2$. Homogenized samples exhibited better corrosion resistance compared to MDF samples. Further, with an increase in the number of MDF passes, $Mg_3Zn_3Gd_2$ volume fraction increased, which led to greater corrosion rates [28]. Bahmani et al. [20] investigated the effect of processing temperature in MDF on XM11 Mg alloy containing 0.59 wt. % Ca and 0.52 wt. % Mn and obtained better tensile properties when processed at 300 °C, whereas better corrosion properties were found at 220–300 °C. However, an increase in the temperature led to an increase in the corrosion rate, and this was attributed to the action of second-phase particles [20].

Nevertheless, several investigations reported that the second-phase particles play a significant role in enhancing the corrosion resistance in the Mg-rare earth alloys. To improve biological properties, different rare earth elements are alloyed with Mg. Among various

rare earth elements, gadolinium (Gd) and neodymium (Nd) showed good improvement in in vitro cytotoxicity behavior [29]. Studies have shown that adding a small amount of Gd and Nd (less than 2 wt. %) as an alloying element does not significantly influence biocompatibility behavior [30,31]. However, the combination of mechanical properties and corrosion resistance is a rare aspect of Mg-rare earth alloys. Indeed, the development of high-strength and corrosion-resistant biocompatible Mg alloys is quite challenging. Therefore, in the current study, the authors attempted to develop high-strength corrosion-resistant Mg alloys for bioimplant applications. For this, a Mg-rare earth alloy, i.e., Mg-Zn-Nd-Gd alloy, has been cast using the stir casting technique and later carried out the MDF till six passes. Further, the microstructural, mechanical, and corrosion properties have been studied. Finally, the effect of MDF processes on microstructures has corroborated corrosion resistance of the Mg-Zn-Nd-Gd alloy.

2. Materials and Methods

2.1. Multi-Directional Forging

The rare earth elements Gd and Nd (99.9 wt. % purity) were procured from metal industries, Mumbai, India. The Mg-Zn-Gd-Nd alloy was synthesized in a mild steel crucible under a protective atmosphere of argon. The chemical composition of the alloy is obtained from spark optical emission spectroscopy (OES), and it is given in Table 1.

Table 1. Chemical Composition of Mg-Zn-Gd-Nd Alloy.

Elements	Zn	Nd	Gd	Zr	Mg
Composition (wt. %)	3.07	1.70	1.40	0.95	Balance

The complete experimental setup details of the MDF are shown in Figure 1a–c. As-received blocks were homogenized as per ASTM B 661 (Standard Practice for Heat Treatment of Magnesium Alloys. ASTM International: West Conshohocken, PA, USA, 2019) at 400 °C for 24 h, followed by air cooling to room temperature. The homogenized Mg-Zn-Gd-Nd alloy blocks were sectioned into small rectangular samples of dimension 30 mm × 30 mm × 20 mm obtained through wire-cut EDM machining. The samples were forged at a uniform strain rate of 2 mm/min at 250 °C. After each pass of MDF, the samples were rotated to their next forging axis, and the same was repeated for the whole cycle. Figure 1d shows the samples processed after MDF under different conditions.

2.2. Microstructural Characterization

The samples for all the microstructure characterizations were extracted from the plane parallel to the final forging axis. The samples were sequentially polished by SiC abrasive papers with different granularities from 120 to 2000 grit size, followed by mechanical buffing using a velvet polishing cloth. To eliminate the scratches induced by mechanical grinding and to prevent the rise in temperature in this process, diamond suspension with a particle size of 1–3 µm, along with kerosene, was also utilized during elaborate polishing.

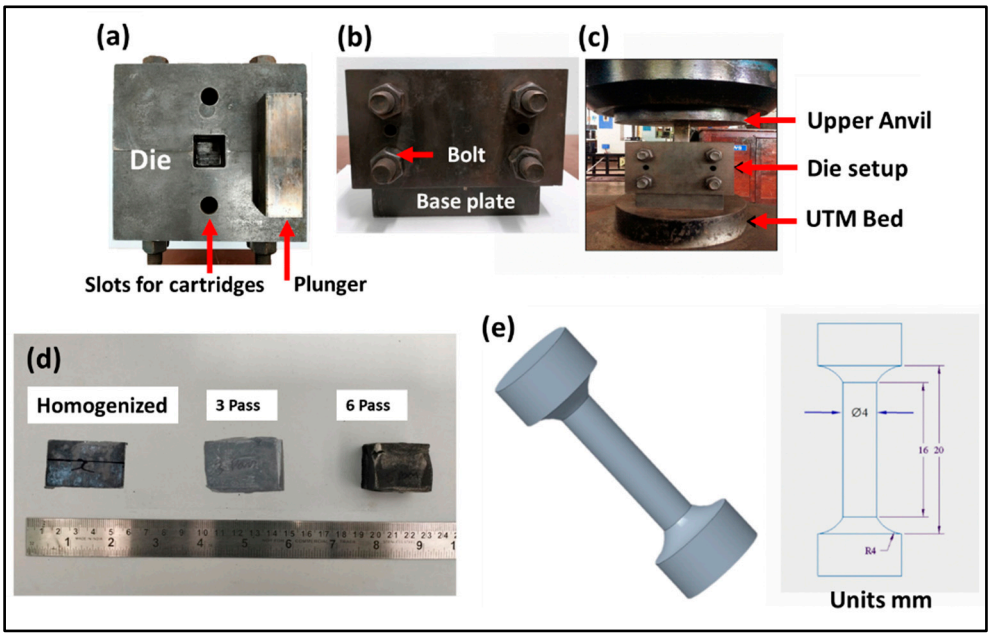


Figure 1. (**a**–**c**) MDF components and (**d**) MDF samples processed at different conditions, and (**e**) tensile sample dimensions.

The samples were etched with a solution containing 10 g oxalic acid + 1 mL nitric acid + 4 mL acetic acid + 200 mL distilled water for 10–20 s. The surface morphology of homogenized, 3-pass, and 6-pass samples was observed using an Optical Microscope (OM, Zeiss, Aixolab A1, Jena, Germany) and Scanning Electron Microscope (SEM, Carl Zesis, Jena, Germany) equipped with EDX. The samples for EBSD were prepared by sequential polishing using SiC abrasive papers from 120 to 2000 grit, followed by electropolishing at 16 V for 60 sec at −25 °C using Struers AC2 electrolyte as per ASTM E1558-09(Standard Guide for Electrolytic Polishing of Metallographic Specimens. ASTM International: West Conshohocken, PA, USA, 2009). The EBSD results were analyzed using the HKL Channel 5 software. X-ray diffraction (XRD) analysis on the homogenized and MDF samples was performed using Empyrean 3rd Gen, Malvern PANalytical diffractometer (Almelo, Netherlands) within the range of 10–110° using Cu-Kα source having a wavelength of 1.54 Å at a scan rate of 5 °/min. The linear intercept method has been employed to measure the grain size.

2.3. Mechanical Properties

Tensile samples were extracted from the blocks of the homogenized and MDF samples as per ASTM E8 standards (Standard Test Methods for Tension Testing of Metallic Materials. ASTM International: West Conshohocken, PA, USA, 2022) with a gauge length of 16 mm. The dimensions of the tensile samples are given in Figure 1e. Tensile testing of 3 samples from each condition (homogenized, 3 pass, and 6 pass) was performed on the universal testing machine (Shimazdu AG-X plus^{TM}, 100 KN, Kyoto, Japan), at a cross-head speed of 1 mm/min at room temperature. Here, the tensile cross-head is parallel to the forging axis. The fracture surface morphology of the ruptured samples was analyzed through SEM. Microhardness test of the homogenized and MDF samples was performed as per ASTM-E384 Standards (Standard Test Method for Microindentation Hardness of Materials. ASTM International: West Conshohocken, PA, USA, 2023) on the Omni Tech Microhardness testing machine. The samples were subjected to a load of 100 gf, and a dwell time of 10 s was employed to calculate the average microhardness for all the samples.

2.4. Electrochemical Corrosion Testing

The electrochemical corrosion studies of the homogenized and MDF samples of dimensions 10 mm × 10 mm × 4 mm in Hank's body solution at 37 ± 0.1 °C were investigated using a traditional three-electrode system in an electrochemical workstation (OrigaFlex chemical workstation). The three-electrode system had a saturated calomel electrode (SCE) as the reference electrode, platinum wire as the counter electrode, and the sample as the working electrode, followed by which the whole three-electrode setup was placed in a water bath at a temperature of 37 ± 0.1 °C. Prior to measuring the open circuit potential (OCP), the samples were immersed for about 5 min in Hank's solution to stabilize potential, and then OCP was measured for about 30 min from −100 to 1000 mV. Electrochemical Impedance Spectroscopy (EIS) measurements were made with a scan rate of 20 mV/sec at the frequency range of 100 KHz to 10 mHz. Potentiodynamic polarization (PDP) tests were then carried out with a scan rate of 1 mV/s after the EIS measurements. From the current density-potential data, Tafel plots were generated. Corrosion rate (mm/yr) was calculated according to ASTM G102 (Standard Practice for Calculation of Corrosion Rates and Related Information from Electrochemical Measurements. ASTM International: West Conshohocken, PA, USA, 2015). The corrosion rate was quantified using the following Equation (1) [32] given below.

$$P_i = 22.85\ I_{Corr} \quad (1)$$

where P_i is corrosion rate in mm/yr and I_{corr} in mA/cm^2.

3. Results and Discussion

3.1. Microstructure and Phase Evolution of the MDF Samples

The OM and SEM microstructures of the homogenized and MDF (three-pass and six-pass) samples are shown in Figures 2 and 3, respectively. The as-cast sample was homogenized at 400 °C for 24 h to obtain uniformity and to dissolve micro irregularities formed during casting and alloying. The homogenized sample exhibited equiaxed honeycomb-shaped grain structure (α-Mg) as shown in Figure 2a with an average grain size of 118 µm ± 5 µm. Further, the grain boundaries were clearly visible and decorated with a continuous eutectic network of second-phase particles along the grain boundaries and fine particles in the grain interior. This can be clear from the SEM microstructures given in Figure 3a. After three passes of MDF, the microstructure exhibited a mixture of coarse and fine grains distributed in an uneven manner (Figure 2b) with an average grain size of 40 ± 10 µm.

Similar observations in the MDF-processed Mg-rare earth alloys were reported by a few researchers [33,34]. The obtained bimodal grain structure formed during MDF at a cumulative strain of ε_3 = 1.2, driven by DDRX. This strain regime promoted partial recrystallization, resulting in a mix of fine DRXed grains (~1–5 µm) and residual coarse grains (~20–110 µm). After six passes of MDF, the grain size was further reduced up to 30 ± 10 µm due to subdivision of grains and the formation of new fine grains inside the grain. It has been observed that with an increase in the cumulative strain (ε_6 = 2.43), grain size decreases. The eutectic network of second-phase particles observed along the grain boundary in the homogenized condition is fragmented during the MDF process, dispersed, and distributed non-uniformly throughout the α-Mg matrix. This can be confirmed from the SEM microstructures provided in Figure 3b,c. These second-phase particles will enhance the DDRX through particle-stimulated nucleation (PSN), leading to formation of fine grains along the grain boundaries and inside the grains [35]. Finally, the microstructure turns into a bimodal grain microstructure, as seen in Figure 2c.

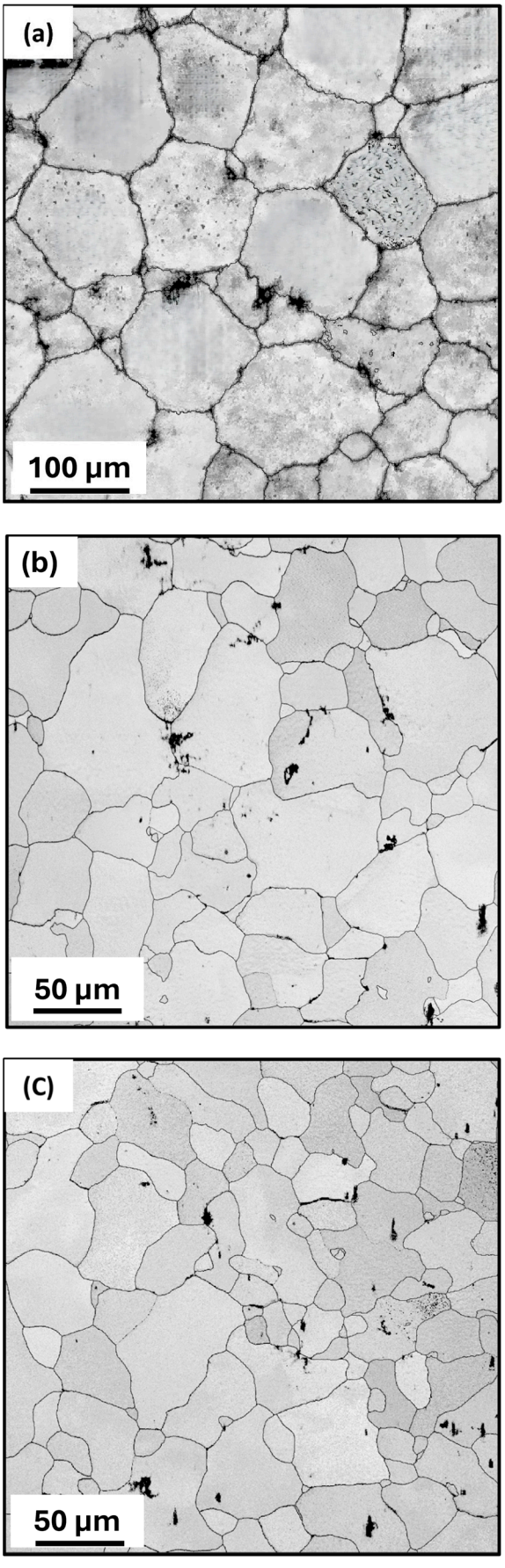


Figure 2. Optical Microstructures: (**a**) homogenized, (**b**) three-pass, and (**c**) six-pass samples.

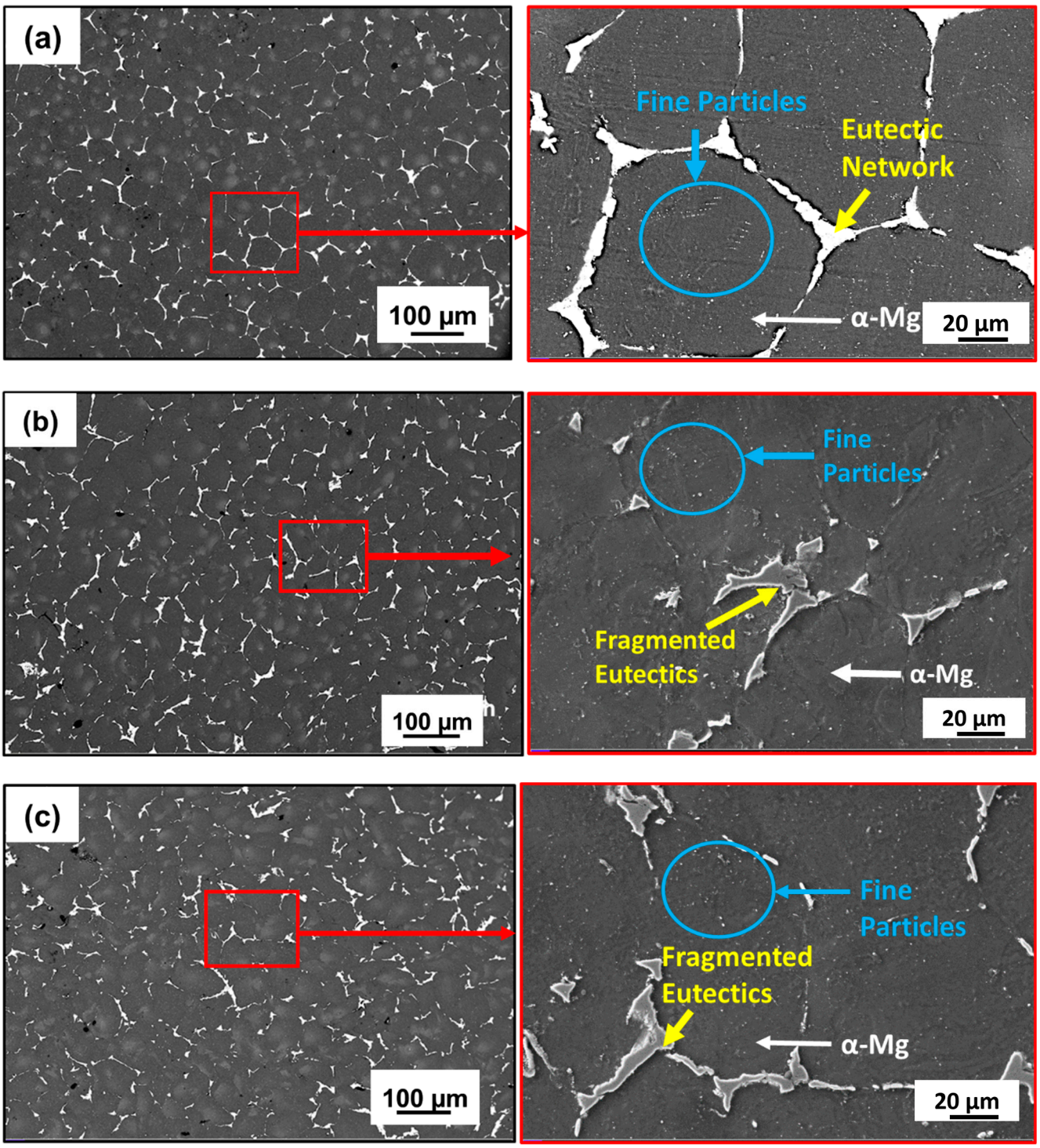


Figure 3. SEM Microstructures: (**a**) homogenized (continuous eutectic network), (**b**) three-pass (semi-continuous eutectic network), and (**c**) six-pass samples (discontinuous eutectic network).

Figure 4 shows the EDS mapping of the homogenized and MDF samples. A higher percentage of α-Mg-rich phases and Zn-Nd-rich secondary phases were present in the microstructure of the Mg-Zn-Gd-Nd alloy, which was supported by the EDS mapping shown in Figure 4a, which revealed a distinct atomic contrast for the elements Mg, Zn, and Nd. The eutectic network of second-phase particles in the homogenized sample had a continuous type of distribution along the grain boundaries, as shown in Figures 3a and 4a. After three passes of MDF, the second-phase particle distribution was found to be semi-

continuous in a uniform manner along the grain boundaries. The presence of very fine second-phase particles near and inside the grain boundaries (Figures 3b and 4b) has also been observed. Further, after six passes of MDF, the second-phase particle distribution was discontinuous along the grain boundaries and was distributed in a non-uniform manner (Figures 3c and 4c). The density of fine second-phase particles was increased compared to three passes, and the same can be reflected in Figures 3c and 4c. This is mainly due to high cumulative strain during the MDF process and leads to the formation of strain-induced precipitation, and similar observations were reported by Cao et al. [28] and Yang et al. [36].

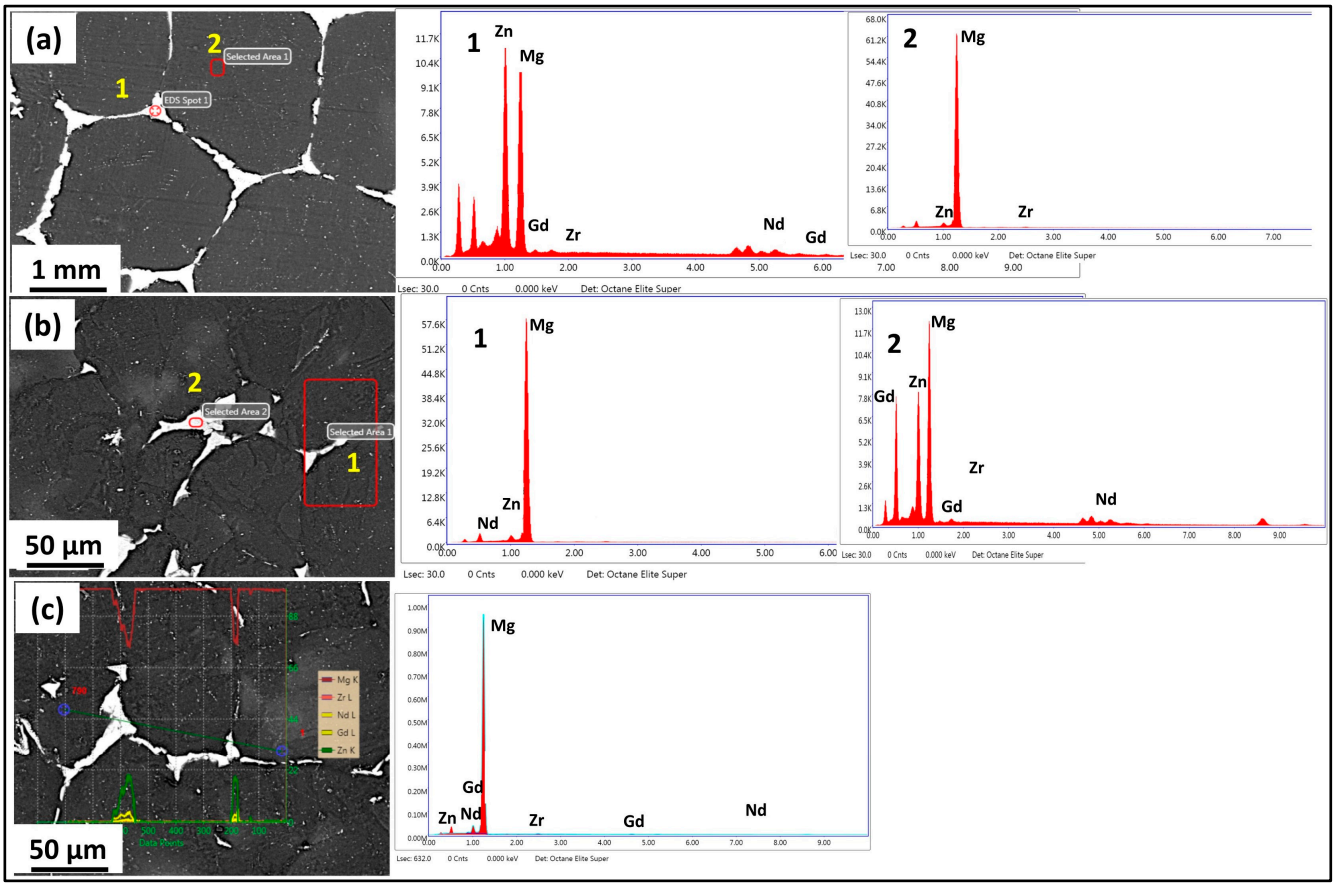


Figure 4. EDS Mapping: (**a**) homogenized, (**b**) 3-pass, and (**c**) 6-pass samples.

Figure 5 shows the XRD patterns of the homogenized and MDF samples. For all three conditions, α-Mg was exhibited as the major phase; however, after the MDF passes, the peaks corresponded to different second-phase particles such as MgZn, Mg_7Zn_3, and $Mg_{12}Nd$. The variation in the intensity of the peaks corresponding to $Mg_{12}Nd$ and Mg_7Zn_3 at different processed conditions can be observed due to the dissolution of particles; further, the major second-phase particles of Mg-Zn-Gd-Nd alloy can be considered as $Mg_{12}Nd$ and Mg_7Zn_3, as observed in XRD and the EDX composition; these observations were consistent with the authors' report in [30,37]. Hence, through XRD phase analysis, it is confirmed that the eutectic network is $Mg_{12}Nd$, and fine second-phase particles are Mg_7Zn_3. Further, no peaks corresponded to the GdZn phase in the six-pass samples due to the dissolution of particles.

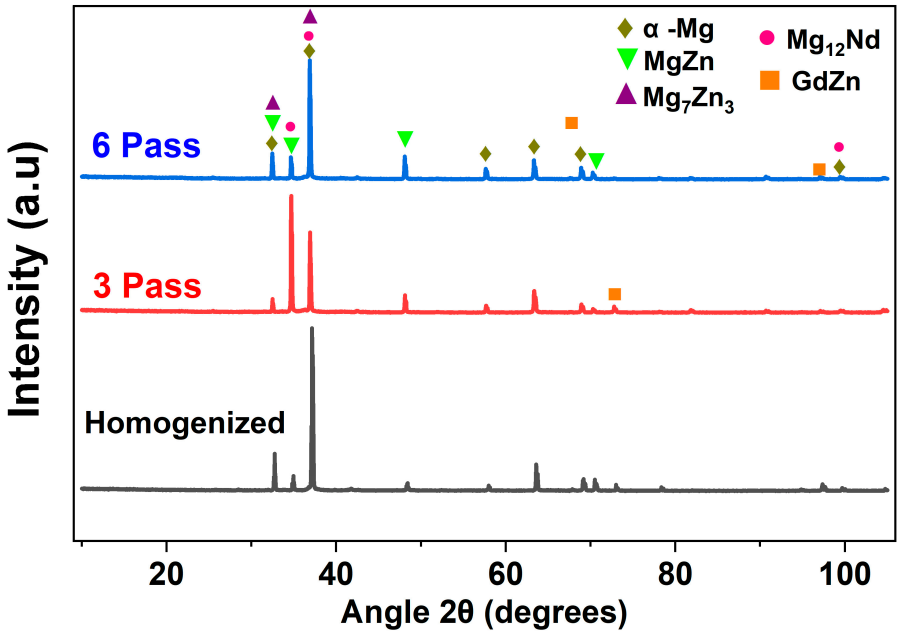
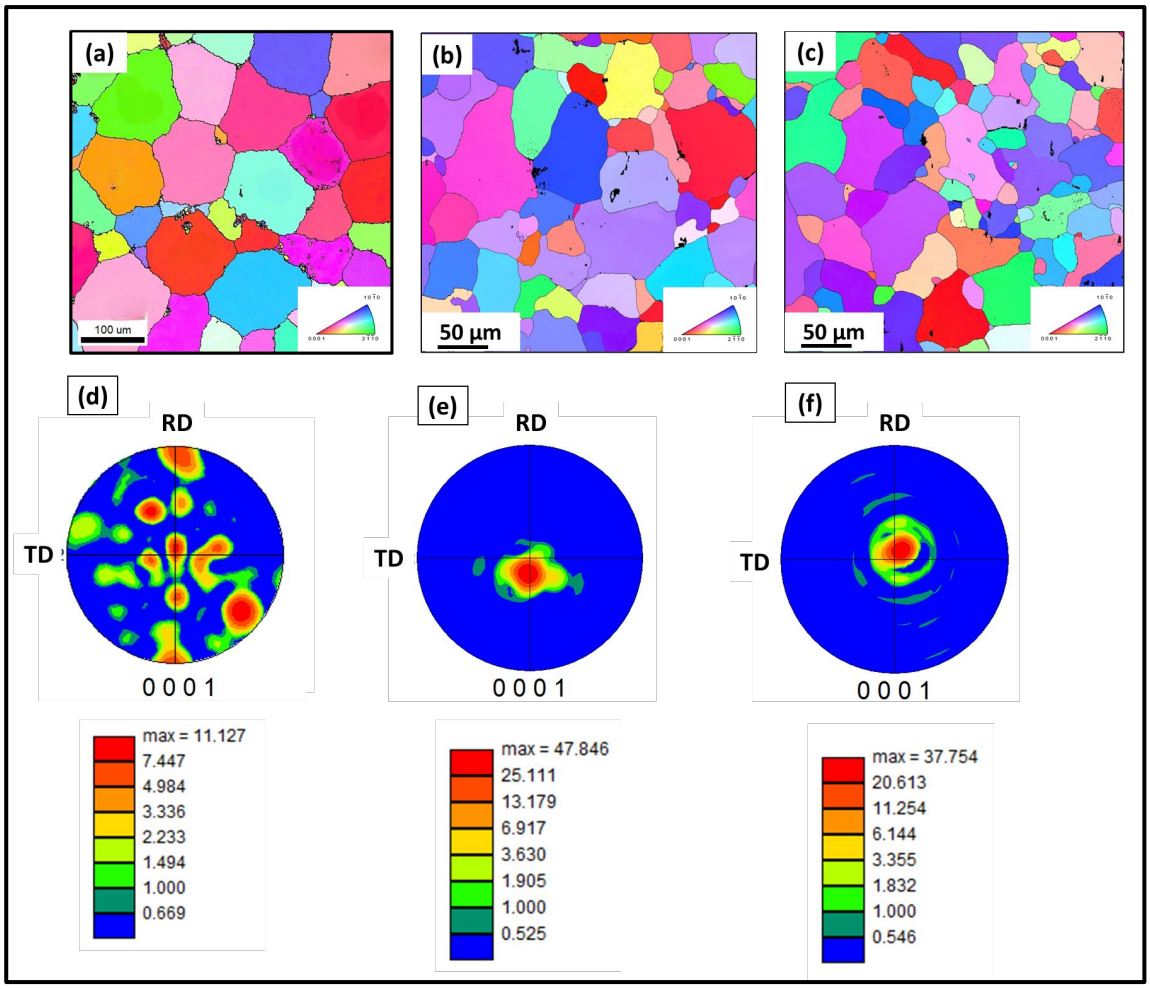


Figure 5. XRD patterns of the homogenized and MDF samples.

Inverse pole figure (IPF) and pole figure (PF) maps were obtained through EBSD analysis of the samples processed at different conditions indicated in Figure 6. It was observed that the homogenized sample exhibited an equiaxed honeycomb-type grain structure with an average grain size of 118 ± 5 μm (Figure 6a). Upon MDF processing, a mixture of both fine and coarse grains, i.e., a bimodal grain structure, was observed in both the three-pass and six-pass samples, and further, no traces of twins were generated (Figure 6b,c). This can be attributed mainly to three possible reasons: (i) the high temperature during MDF, (ii) the orientation of grains during deformation that restricted the twinning activation, and (iii) reduction in grain size (for three pass 40 ± 10 μm and for six pass 30 ± 10 μm) upon increase in strain accumulation with increase in MDF passes. However, a significant reduction in grain size was observed after the MDF passes. Primarily, a random texture (Figure 6d) was observed in the homogenized sample. After MDF, the random texture turned into a near-net strong basal texture. The basal (0001) PFs (Figure 6e,f) confirm the presence of texture but are slightly weakened along the basal plane (0002) after the MDF passes. The presence of random texture in the Mg-rare earth alloys after SPD is quite common and widely reported [38–41].

The distribution of grain boundary misorientation angles is presented in Figure 6g. A marked increase in the fraction of LAGBs (1–15°) is observed in the MDF-processed samples, rising from 48% in the homogenized condition to 84% post-processing. This increase is primarily attributed to the formation of fine sub-grains and a high density of dislocations generated during the MDF process. Concurrently, a significant reduction in the fraction of HAGBs (15–180°) is observed, decreasing from 52% in the homogenized sample to 17% in the MDF-processed samples. Notably, the maximum fraction of HAGBs was found in the homogenized condition. The higher fraction of HAGBs in the homogenized sample is known to enhance corrosion resistance in Mg-rare earth alloys [38], a point that will be further discussed in Section 3.3 on corrosion behavior.



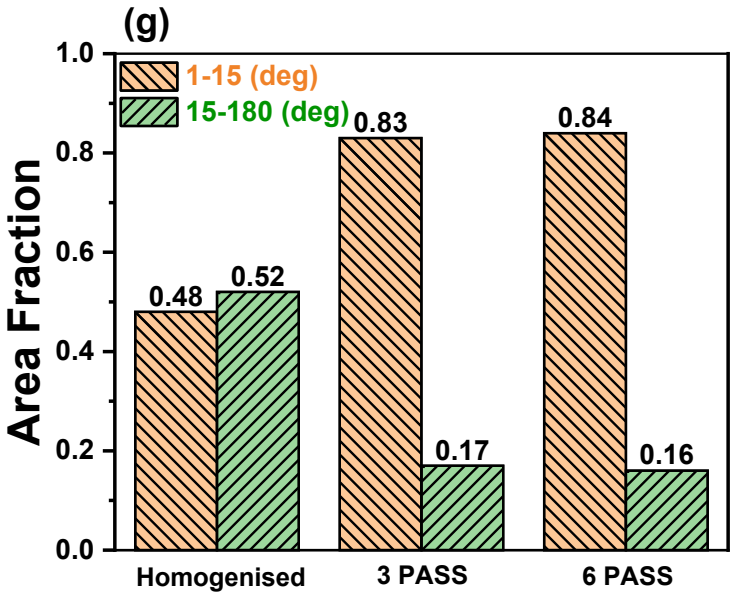


Figure 6. Inverse pole figures: (**a**) homogenized, (**b**) 3-pass, and (**c**) 6-pass samples; pole figures: (**d**) homogenized, (**e**) 3-pass, (**f**) 6-pass samples, and (**g**) grain boundary misorientation distribution.

3.2. Mechanical Response

3.2.1. Tensile Behavior and Fracture Analysis

Engineering stress–strain curves of the homogenized and MDF samples are plotted in Figure 7a. Figure 7b summarizes the mechanical properties of samples processed at

different conditions. It was observed that the YS, UTS, and % of elongation were increased with increasing number of MDF passes. The YS and UTS of the homogenized sample were 96 ± 3 MPa and 151 ± 4 MPa, respectively. The maximum UTS was observed in the six-pass sample (250 ± 7 MPa), followed by three-pass (219 ± 6 MPa), and then homogenized (151 ± 4 MPa). A similar trend was observed in the YS and % elongation of the six-pass sample. Indeed, it was noticed that overall, a 59% increase in UTS, 92% increase in YS, and 40% increase in elongation were observed in the six-pass sample compared to the homogenized sample. This unique combination of highest strength and ductility was significant and very special for bioimplant applications [42]. The increase in the YS and UTS after MDF can be primarily attributed to MDF-induced grain refinement due to high strain accumulation and dispersion strengthening from second-phase particles $Mg_{12}Nd$ and Mg_7Zn_3 [43,44]. After six passes of MDF, the continuous eutectic network had fragmented into discontinuous particles and distributed non-uniformly in the α-Mg matrix. This could restrict the premature failure of the sample and enhance the ductility. Further, the significant enhancement in the elongation of the three- and six-pass samples is primarily attributed to the weak basal texture observed in Figure 6e,f obtained after the MDF process. The weakening of texture in Mg-rare earth alloys helps in enhancing the ductility of samples. This phenomenon is well addressed and documented by the researchers and authors' previous findings [39,40]. In addition, the MDF samples exhibited outstanding elongation because activation of different slip systems that are introduced after texture randomization really boosted the elongation [45,46].

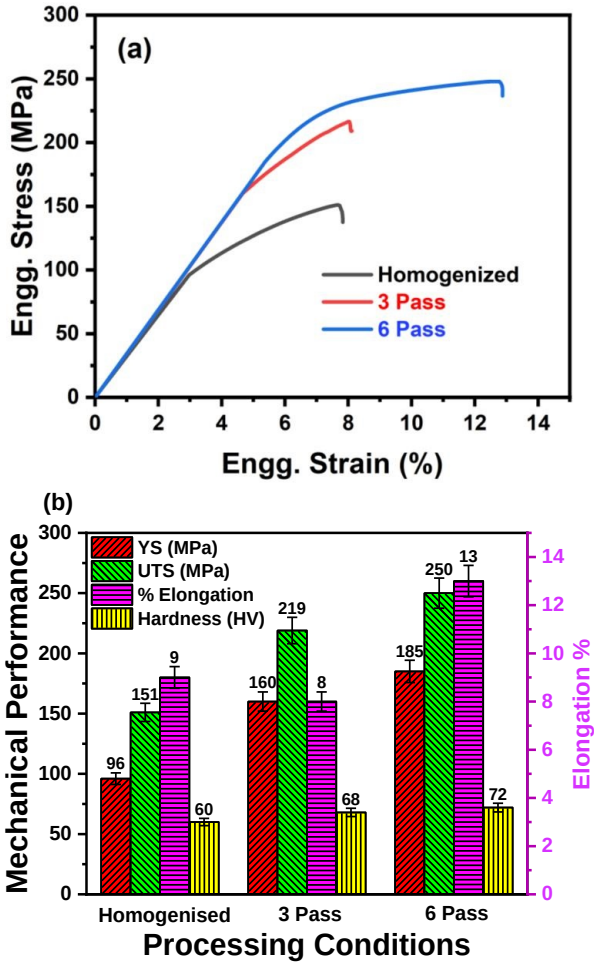


Figure 7. (**a**) Engineering stress–strain curve of the samples processed at different conditions, and (**b**) comparison of UTS and elongation % of the samples processed at different conditions.

3.2.2. Microhardness Evolution

The microhardness results of the samples processed under different conditions are presented in Figure 7b. The homogenized sample exhibited an average microhardness of 60 ± 1 HV, which was the lowest among all the conditions. A notable increase in microhardness was observed after MDF of the Mg-Zn-Nd-Gd alloy. Specifically, the samples processed through three and six passes exhibited average microhardness values of 68 ± 1.2 HV and 72 ± 1.7 HV, respectively. However, the increase from three to six passes was relatively modest, which can be attributed to the complete dissolution of the GdZn phase after six passes, as confirmed by the XRD analysis (Figure 5). Overall, the MDF process led to an enhancement of approximately 20% in microhardness compared to the homogenized condition. This improvement can be primarily ascribed to grain refinement (Figure 6), strain hardening, and dispersion strengthening resulting from the presence of secondary phase particles such as $Mg_{12}Nd$ and Mg_7Zn_3 along both the grain boundaries and interiors of the MDF-processed samples [47].

Figure 8 reveals the fracture surface of the homogenized and MDF samples. The homogenized sample fracture surfaces revealed tearing ridges and micro cracks leading to macro-ones (Figure 8a). The presence of a tearing edge and cleavage facets is an indication of brittle fracture. The convergence of certain micro cracks to macro crack, leading to the formation of a tearing edge, has been observed (Figure 8a). Mg alloys usually have a brittle type of failure due to the restricted dislocation system; the formation of the cleavage facets can be attributed to the presence of large α-Mg grains [48]. However, the sample processed for three passes exhibited the presence of dimples of different dimensions and also a river-like pattern, as shown in Figure 8b. This indicates that the three-pass sample showed a mixed mode of fracture (brittle + ductile) with a considerable percentage of elongation. This can be attributed to the grain refinement because of MDF processing. Reduction in tearing edges and the size of dimples was observed in the sample processed up to six passes, as shown in Figure 8c. Compared to the three-pass and six-pass samples, it had a greater grain refinement in microstructure; as a result, the reduction in dimple size and increase in elongation percentage could be observed. Fracture of the samples processed at six passes is a combination of brittle and ductile fracture, and is more dominated by a ductile nature. The depth of the dimple depends on the microstructure and plasticity of the material [49,50].

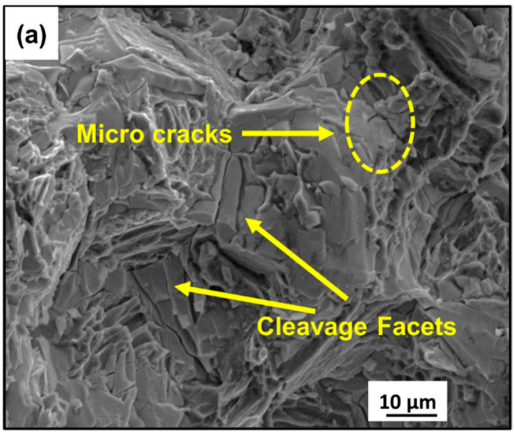


Figure 8. *Cont.*

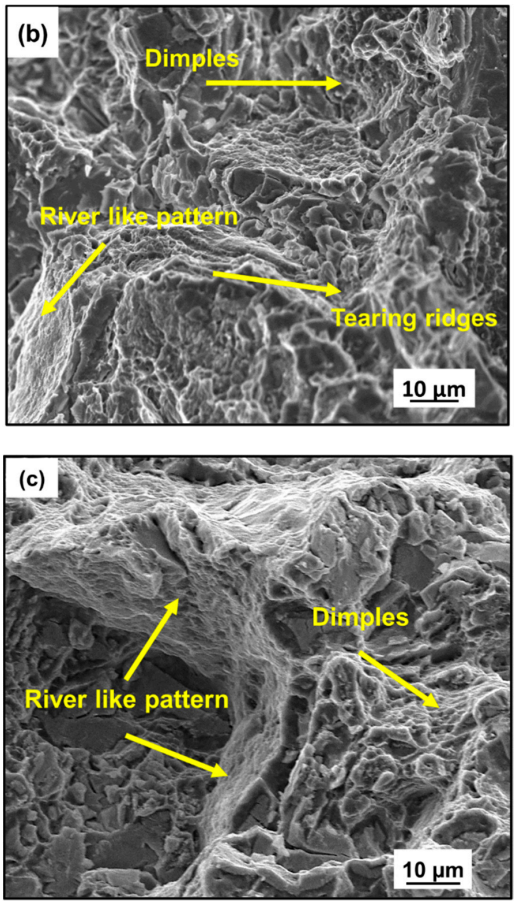


Figure 8. Fractography images: (**a**) homogenized, (**b**) 3-pass, and (**c**) 6-pass samples.

3.3. Electrochemical Corrosion Behavior

3.3.1. Potentiodynamic Polarization (PDP) Studies

PDP curves of the homogenized and MDF samples tested at 37 ± 1 °C in Hank's body solution are plotted in Figure 9a. The measured parameters, such as corrosion potential (E_{corr}), corrosion current density (I_{corr}), anodic slope (βa), and cathodic slope (βc), were calculated from Tafel plots and are tabulated in Table 2. From Table 2, it can be inferred that the corrosion rate increased after the MDF process. However, the corrosion current density is directly proportional to the corrosion density; with an increase in corrosion current, the corrosion rate also increases. The cathodic curve represents the evolution of hydrogen when subjected to corrosion, whereas the anodic curve represents the dissolution of Mg. All the samples have similar polarization curve trends, having a steep increase in anode curves due to the negative difference effect. The PDP results reveal that the homogenized sample exhibits the most noble corrosion potential (−1.2799 V) and the lowest corrosion current density (0.0051 mA cm^{-2}), while the three-pass MDF specimen shows the highest corrosion current density (0.0199 mA cm^{-2}) and the least charge-transfer resistance (34.9 ohm·cm^2) derived from the EIS analysis. The six-pass sample shows an intermediate behavior (I_{corr} = 0.0109 mA cm^{-2}; R_t = 144.5 Ω·cm^2). These variations are consistent with the microstructural evolution during MDF, which modifies grain-boundary character, texture, and intermetallic distribution. Table 2 shows that the homogenized sample had a lower corrosion rate of 0.1165 mm/yr compared to the three- and six-pass samples. From Figure 9a, it is observed that the homogenized sample exhibited the filiform type of corrosion, and a small part is affected by pitting corrosion. The area fraction of HAGBs is maximum (55%) for the homogenized sample. A passive layer is formed due to the high fraction of HAGBs, which could enhance the corrosion resistance for the

homogenized sample [51]. After three and six passes of MDF, corrosion potential shifted to −1.2967 and −1.1999, respectively, which is decreased slightly with an increase in corrosion current density compared to the homogenized sample, hence having a slightly higher corrosion rate of 0.4560 mm/yr and 0.2499 mm/yr for three and six passes, respectively. In strongly textured Mg alloys, Song et al. [51] noticed that surfaces that had higher {0002} basal planes exhibited more corrosion resistance than those with lesser basal planes. In addition, Xin et al. [52] had investigated the effect of texture on corrosion behavior of AZ31 Mg alloy, and observed similar results, which were noticed by Song et al. Here, the MDF samples exhibited near-net strong basal texture (weak texture), and the presence of high discontinuous distribution of LAGBs could lead to galvanic corrosion attack at the grain boundaries. Grain boundaries and LAGBs exhibit more active sites and energy compared to the substrate, which acts as a highly active site. Consequently, grain refining enhances the area of grain boundaries and LAGBs, resulting in an enhanced dissolution rate of atoms at the grain boundaries and augmenting the chemical reactivity of the alloy [53]. In addition, Cui et al. [54] studied the effect of grain size and second-phase particles on the corrosion behavior of Mg-3Al-5Pb-1Ga-Y alloy. They found that the presence of a high fraction of LAGBs and fine second-phase particles enhanced the corrosion rate. After three passes, the bimodal grain structure (coarse unrecrystallized + fine DRXed grains) introduced moderate surface energy heterogeneity, with corrosion initiating preferentially at fine-grained regions (higher energy). The further refined microstructure increased the total grain boundary area and surface free energy after six passes, leading to a more pronounced corrosion rate. The presence of high fraction of grain boundary is further confirmed with the grain boundary distribution presented in Figure 6g. The weakened texture also reduced the fraction of corrosion-resistant basal planes, exacerbating material degradation [55].

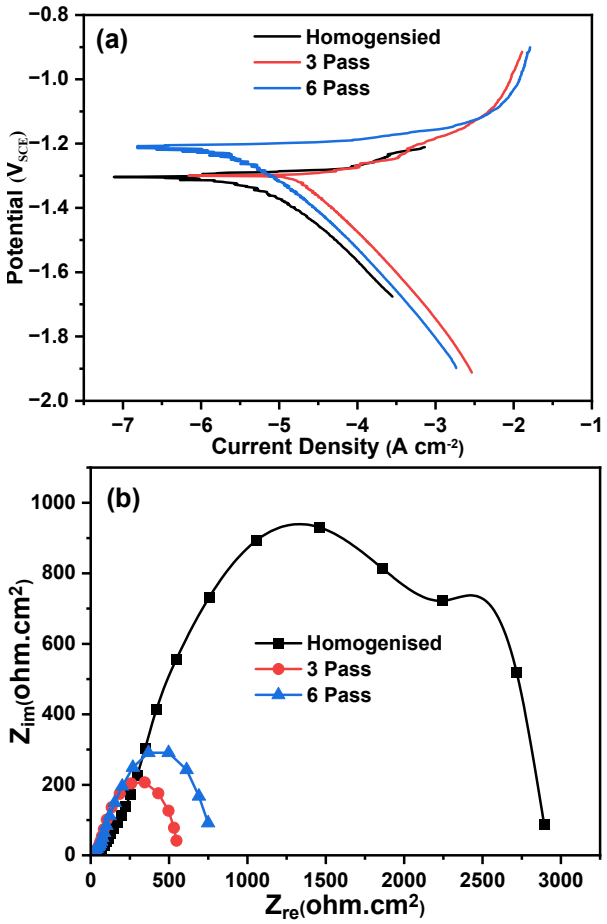


Figure 9. *Cont.*

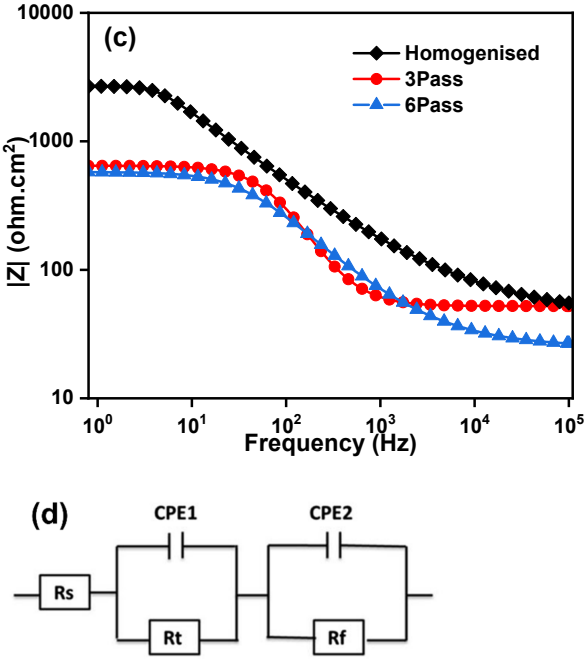


Figure 9. (**a**) PDP curves, (**b**) Nyquist plot, (**c**) Bode plots of samples processed at different conditions, and (**d**) equivalent EIS circuit.

Table 2. Corrosion Properties of The Samples Processed at Different Conditions.

Sample Condition	I_{corr} (mA/cm^2)	E_{corr} (V)	βa	βc	CR (mm/yr)
Homogenized	0.0051	−1.2799	0.0071	−0.1987	0.1165
3 Pass	0.0199	−1.2967	0.0285	−0.2557	0.4560
6 Pass	0.0109	−1.1999	0.0044	−0.2606	0.2499

3.3.2. Electrochemical Impedance Spectroscopy

Nyquist and Bode plots of the homogenized and MDF samples in Hank's body solution at 37 ± 0.1 °C are shown in Figure 9b,c. EIS provides the inductive and capacitance loop and is also used to investigate the electrochemical interface between the electrode and electrolytes. The Nyquist plot depicts a semicircle, which indicates the capacitance arc and the formation of protective film and degradation of it. The capacitance arc's diameter represents the corrosion resistance of Mg-Zn-Gd-Nd alloy. From Figure 9b, it can be observed that all the samples exhibited depressed semicircles; also, the homogenized sample had a larger semicircle, followed by the six- and three-pass samples, indicating better corrosion resistance for the homogenized sample. The equivalent circuit used to analyze the Nyquist is shown in Figure 9c. High frequency capacitive loop of the electrode reaction process was described using a parallel circuit of electric double-layer capacitance cell (C_{dl}) and charge transfer (R_t). Constant phase elements (CPE1 and CPE2) and a film resistance R_f were introduced to the circuit. If the metals exhibit better corrosion resistance, it is difficult to transfer charges between the solution and the sample surface, so R_t becomes higher. It is noticed that, R_t values for the homogenized, three-pass, and six-pass samples are 244.5 ohm·cm^2, 34.9 ohm·cm^2, and 144.5 ohm·cm^2, respectively. Therefore, the corrosion resistance for the homogenized sample increased when compared to the MDF samples.

Micro-galvanic coupling between the α-Mg matrix and intermetallic phases ($Mg_{12}Nd$ and Mg_7Zn_3) plays a decisive role. The homogenized alloy shows relatively coarse and semi-continuous $Mg_{12}Nd$ at grain boundaries, while MDF processing refines and redistributes these particles. The fine, discontinuous precipitates formed after three passes

provide numerous cathodic sites adjacent to the α-Mg matrix, enhancing micro-galvanic interactions and accelerating localized dissolution. Consequently, the three-pass specimen records a higher I_{corr} and lower R_t. Such particle-induced galvanic effects have been widely reported in Mg–Nd and Mg–Zn alloys, where the electrochemical potential difference between intermetallics and the Mg matrix determines local corrosion kinetics [56,57]. The corrosion rate of the MDF-processed samples up to three passes has declined compared to the homogenized sample. However, there is a slight decrease in corrosion rate of six-pass samples compared to three-pass samples, and the primary reason can be attributed to the type, phase, and distribution of the second-phase particles present in the microstructure. However, the corrosion resistance depends on the electrode potential of the matrix and the adjoining phases. The majority of the second-phase particles identified through EDX and XRD is $Mg_{12}Nd$ and Mg_7Zn_3 (Figure 4b,c) and Figure 5; these phases will corrode first if the potential of the phase is lower than that of the substrate. From Figure 10, it is noticed that the three- and six-pass samples have experienced pitting corrosion. The corrosion potential of second-phase particles is lower than the Mg substrate, so that the second-phase particles acted as an anode and dissolved preferentially [58]. However, as reported in the microstructure results, the distribution of the second-phase particles $Mg_{12}Nd$ was continuous among the grain boundaries in the homogenized sample, whereas semi-continuous with respect to the three- and six-pass samples. Therefore, it cannot provide better protection to the substrate if its distribution is discontinuous. The corrosion resistance of Mg alloy is closely related to the length of the grain boundary, which acts as a physical barrier [59]. The fragmented fine second-phase particles act as a cathode near the LAGBs, and the α-Mg matrix acts as an anode, which forms a micro galvanic couple. From Figure 10b,c, it is observed that pitting corrosion occurred at the grain boundaries region for both samples due to the severe galvanic effect, which could increase the corrosion rate after MDF on Mg-Zn-Nd-Gd alloy.

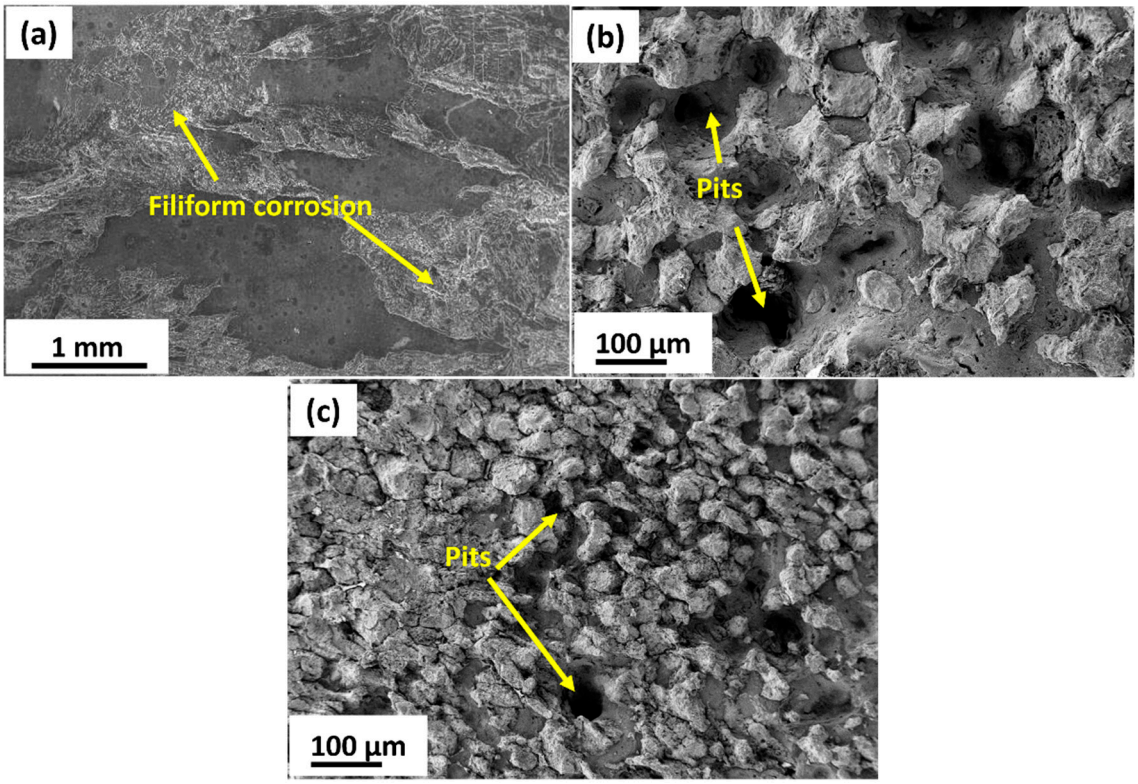


Figure 10. Surface morphologies after corrosion testing: (**a**) homogenized, (**b**) 3-pass, and (**c**) 6-pass samples.

4. Conclusions

The biodegradable homogenized Mg-Zn-Gd-Nd alloy was successfully processed through MDF up to six passes at 250 °C with a cumulative strain of 2.43. Mechanical and microstructural characterizations were carried out to study the effect of MDF on the Mg-Zn-Gd-Nd alloy. To evaluate its suitability for biomedical applications, the corrosion behavior of the alloy was analyzed in Hank's body solution at 37 °C under various processing conditions. Key findings from the study are summarized below:

Grain size reduced from 118 ± 5 μm in the homogenized condition to 30 ± 10 μm after six passes with uniform distribution of Mg_7Zn_3 fine particles and semi-continuous $Mg_{12}Nd$ eutectic network.

The microhardness of the six-pass MDF sample increased by 20%, while UTS and YS exhibited significant enhancements of 59% and 90%, respectively, compared to the homogenized sample. This is due to the fact that the grain refinement, strain hardening, and dispersion strengthening from the second-phase particles.

Additionally, the ductility of the six-pass MDF sample improved remarkably, with a 44% increase in elongation, attributed to texture weakening and uniform second-phase distribution (resisting premature failure).

The homogenized sample exhibited better corrosion resistance compared to MDF-processed samples. Although the corrosion rate of the six-pass MDF-processed sample (0.2499 mm/yr) is higher than that of the homogenized samples (0.1165 mm/yr), this remains within an acceptable range for biodegradable implant applications.

The slight reduction in corrosion resistance of the MDF-processed samples can be attributed to a high fraction of LAGBs and fine second-phase particles; however, it does not compromise the alloy's suitability for biomedical use. Instead, the controlled degradation rate aligns well with the clinical requirements for biodegradable implants, where gradual material dissolution is essential for tissue regeneration.

Author Contributions: Conceptualization, F.K.M., U.R. and S.M.A.K.M.; methodology, U.R., S.Q.M. and R.M.; software, H.A., R.M. and S.M.A.K.M.; validation, H.A., S.Q.M.,R.M. and S.M.A.K.M.; formal analysis, S.Q.M., R.M. and S.M.A.K.M.; investigation, F.K.M., U.R., and R.M.; resources, F.K.M., U.R., R.M. and H.A.; data curation, F.K.M., S.Q.M. and S.M.A.K.M.; writing—original draft preparation, F.K.M., U.R. and S.M.A.K.M.; writ-ing—review and editing, F.K.M., U.R., and S.M.A.K.M.; visualization, H.A., S.Q.M. and R.M.; supervision, F.K.M., U.R., and S.M.A.K.M.; project administration, F.K.M., U.R., and H.A.; funding acquisition, F.K.M., H.A. and S.Q.M. All authors have read and agreed to the published version of the manuscript.

Funding: This work was supported by the Deanship of Scientific Research, Vice Presidency for Graduate Studies and Scientific Research, King Faisal University, Saudi Arabia. Grant No. KFU253230.

Institutional Review Board Statement: Not applicable.

Informed Consent Statement: Not applicable.

Data Availability Statement: The original contributions presented in the study are included in the article, further inquiries can be directed to the corresponding author.

Conflicts of Interest: The authors declare no conflict of interest.

References

1. Zheng, L.; Zhao, S.; Li, Y.; Xu, J.; Yan, W.; Guo, B.; Xu, J.; Jiang, L.; Zhang, Y.; Wei, H.; et al. Engineered MgO nanoparticles for cartilage-bone synergistic therapy. *Sci. Adv.* **2024**, *10*, eadk6084. [CrossRef]
2. Zan, R.; Shen, S.; Huang, Y.; Yu, H.; Liu, Y.; Yang, S. Smart Materials in Medicine Research hotspots and trends of biodegradable magnesium and its alloys. *Smart Mater. Med.* **2023**, *4*, 468–479. [CrossRef]

3. Kačarević, Ž.P.; Rider, P.; Elad, A.; Tadic, D.; Rothamel, D.; Sauer, G.; Bornert, F.; Windisch, P.; Hangyási, D.B.; Molnar, B.; et al. Biodegradable magnesium fixation screw for barrier membranes used in guided bone regeneration. *Bioact. Mater.* **2022**, *14*, 15–30. [CrossRef]
4. Wei, H.; Wee, D.; Toong, Y.; Chen, J.; Ng, K.; Ow, V.; Lu, S.; Poh, L.; En, P.; Wong, H.; et al. Polymer blends and polymer composites for cardiovascular implants. *Eur. Polym. J.* **2021**, *146*, 110249. [CrossRef]
5. Prakasam, M.; Locs, J.; Salma-Ancane, K.; Loca, D.; Largeteau, A.; Berzina-Cimdina, L. Biodegradable Materials and Metallic Implants—A Review. *J. Funct. Biomater.* **2017**, *8*, 44. [CrossRef]
6. Kumar, K.; Gill, R.S.; Batra, U. Challenges and opportunities for biodegradable magnesium alloy implants. *Mater. Technol.* **2018**, *33*, 153–172. [CrossRef]
7. Song, G. Control of biodegradation of biocompatable magnesium alloys. *Corros. Sci.* **2007**, *49*, 1696–1701. [CrossRef]
8. Li, Z.; Gu, X.; Lou, S.; Zheng, Y. The development of binary Mg-Ca alloys for use as biodegradable materials within bone. *Biomaterials* **2008**, *29*, 1329–1344. [CrossRef]
9. Mehdizade, M.; Eivani, A.R.; Esmaielzadeh, O.; Tabatabaei, F. Fabrication of osteogenesis induced WE43 Mg-Hydroxyapatite composites with low biodegradability and increased biocompatibility for orthopedic implant applications. *J. Mater. Res. Technol.* **2023**, *25*, 4277–4298. [CrossRef]
10. Gu, X.N.; Li, S.S.; Li, X.M.; Fan, Y.B. Magnesium based degradable biomaterials: A review. *Front. Mater. Sci.* **2014**, *8*, 200–218. [CrossRef]
11. Cao, F.; Song, G.L.; Atrens, A. Corrosion and passivation of magnesium alloys. *Corros. Sci.* **2016**, *111*, 835–845. [CrossRef]
12. Atrens, A.; Shi, Z.; Mehreen, S.U.; Johnston, S.; Song, G.; Chen, X.; Pan, F. Review of Mg alloy corrosion rates. *J. Magnes. Alloys* **2020**, *8*, 989–998. [CrossRef]
13. Zhao, M.C.; Zhao, Y.C.; Yin, D.F.; Wang, S.; Shangguan, Y.M.; Liu, C.; Tan, L.L.; Shuai, C.J.; Yang, K.; Atrens, A. Biodegradation Behavior of Coated As-Extruded Mg–Sr Alloy in Simulated Body Fluid. *Acta Metall. Sin. Engl. Lett.* **2019**, *32*, 1195–1206. [CrossRef]
14. Razzaghi, M.; Kasiri-Asgarani, M.; Bakhsheshi-Rad, H.R.; Ghayour, H. In Vitro Degradation, Antibacterial Activity and Cytotoxicity of Mg-3Zn-xAg Nanocomposites Synthesized by Mechanical Alloying for Implant Applications. *J. Mater. Eng. Perform.* **2019**, *28*, 1441–1455. [CrossRef]
15. Gungor, A.; Incesu, A. Effects of alloying elements and thermomechanical process on the mechanical and corrosion properties of biodegradable Mg alloys. *J. Magnes. Alloys* **2021**, *9*, 241–253. [CrossRef]
16. Yamasaki, Y.; Yoshida, Y.; Okazaki, M.; Shimazu, A.; Kubo, T.; Akagawa, Y.; Uchida, T. Action of FGMgCO$_3$Ap-collagen composite in promoting bone formation. *Biomaterials* **2003**, *24*, 4913–4920. [CrossRef]
17. Rokkala, U.; Jana, A.; Bontha, S.; Ramesh, M.R.; Balla, V.K. Comparative investigation of coating and friction stir processing on mg-Zn-Dy alloy for improving antibacterial, bioactive and corrosion behaviour. *Surf. Coat. Technol.* **2021**, *425*, 127708. [CrossRef]
18. Khan, M.F.; Rokkala, U. Development of high strength and corrosion resistance Mg-Zn-Dy/HA-Ag composite for temporary implant applications. *Mater. Lett.* **2023**, *347*, 134604. [CrossRef]
19. Prithivirajan, S.; Narendranath, S.; Desai, V. Analysing the combined effect of crystallographic orientation and grain refinement on mechanical properties and corrosion behaviour of ECAPed ZE41 Mg alloy. *J. Magnes. Alloys* **2020**, *8*, 1128–1143. [CrossRef]
20. Bahmani, A.; Arthanari, S.; Shin, K.S. Achieving a high corrosion resistant and high strength magnesium alloy using multi directional forging. *J. Alloys Compd.* **2021**, *856*, 158077. [CrossRef]
21. Kumar, A.; MD, F.K.; Panigrahi, S.K.; Chaudhari, G.P. Microstructural evolution and corrosion behaviour of friction stir-processed QE22 magnesium alloy. *Corros. Rev.* **2021**, *39*, 351–360. [CrossRef]
22. Sun, L.; Li, F.; Zhang, J.Y.; Niu, W.T.; Cao, M.Z. Mechanism of work hardening and softening behavior of AZ31 magnesium alloy sheets with hard plate accumulative roll bonding. *J. Magnes. Alloys* **2024**, *13*, 3430–3449. [CrossRef]
23. Ebrahimi, M.; Wang, Q.; Attarilar, S. A comprehensive review of magnesium-based alloys and composites processed by cyclic extrusion compression and the related techniques. *Prog. Mater. Sci.* **2023**, *131*, 101016. [CrossRef]
24. Miura, H.; Yang, X.; Sakai, T. Evolution of Ultra-Fine Grains in AZ31 and AZ61 Mg Alloys during Multi Directional Forging and Their Properties Temperature/K (b) Single pass. *Mater. Trans.* **2008**, *49*, 1015–1020. [CrossRef]
25. Zhang, Z.; Yuan, L.; Zheng, M.; Wei, Q.; Shan, D.; Guo, B. Achievement of high strength and good ductility in the large-size AZ80 Mg alloy using a designed multi-directional forging process and aging treatment. *J. Mater. Process. Technol.* **2023**, *311*, 117828. [CrossRef]
26. Anne, G.; Sampath, R.; Kumar, G. Development, Characterization, Mechanical and Corrosion Behaviour Investigation of Multi-direction Forged Mg–Zn Alloy. In *Magnesium Technology 2019*; Springer: Berlin/Heidelberg, Germany, 2019. [CrossRef]
27. Ramesh, S.; Anne, G.; Nayaka, H.S.; Sahu, S.; Ramesh, M.R. Influence of Multidirectional Forging on Microstructural, Mechanical, and Corrosion Behavior of Mg-Zn Alloy. *J. Mater. Eng. Perform.* **2019**, *28*, 2053–2062. [CrossRef]
28. Cao, F.; Deng, K.; Nie, K.; Kang, J.; Niu, H. Microstructure and corrosion properties of Mg-4Zn-2Gd-0.5Ca alloy influenced by multidirectional forging. *J. Alloys Compd.* **2019**, *770*, 1208–1220. [CrossRef]

29. Feyerabend, F.; Fischer, J.; Holtz, J.; Witte, F.; Willumeit, R.; Drücker, H.; Vogt, C.; Hort, N. Evaluation of short-term effects of rare earth and other elements used in magnesium alloys on primary cells and cell lines. *Acta Biomater.* **2010**, *6*, 1834–1842. [CrossRef]
30. Kottuparambil, R.R.; Bontha, S.; Rangarasaiah, R.M.; Arya, S.B.; Jana, A.; Das, M.; Balla, V.K.; Amrithalingam, S.; Prabhu, T.R. Effect of zinc and rare-earth element addition on mechanical, corrosion, and biological properties of magnesium. *J. Mater. Res.* **2018**, *33*, 3466–3478. [CrossRef]
31. Myrissa, A.; Braeuer, S.; Martinelli, E.; Willumeit-Römer, R.; Goessler, W.; Weinberg, A.M. Gadolinium accumulation in organs of Sprague–Dawley® rats after implantation of a biodegradable magnesium-gadolinium alloy. *Acta Biomater.* **2017**, *48*, 521–529. [CrossRef]
32. Zhao, M.-C.; Liu, M.; Song, G.-L.; Atrens, A. Influence of pH and chloride ion concentration on the corrosion of Mg alloy ZE41. *Corros. Sci.* **2008**, *50*, 3168–3178. [CrossRef]
33. Li, J.; Han, Q.; Han, X.; Yi, X. Strength—Ductility synergy in Mg-Gd-Y-Zr alloys via texture engineering in bi-directional forging. *J. Magnes. Alloys* **2024**, *12*, 4709–4721. [CrossRef]
34. Wang, R.; Yan, F.; Sun, J.; Xing, W.; Li, S. Microstructural Evolution and Mechanical Properties of Extruded AZ80 Magnesium Alloy during Room Temperature Multidirectional Forging Based on Twin Deformation Mode. *Materials* **2024**, *17*, 5055. [CrossRef]
35. Mohammed, S.M.A.K.; Nisar, A.; John, D.; Sukumaran, A.K.; Fu, Y.; Paul, T.; Hernandez, A.; Seal, S.; Agarwal, A. Boron nitride nanotubes induced strengthening in aluminum 7075 composite via cryomilling and spark plasma sintering. *Adv. Compos. Hybrid Mater.* **2025**, *8*, 155. [CrossRef]
36. Yang, S.; Sun, Z.; Wang, Z.; Zhao, S.; Wang, K.; Li, D.; Wang, X. Microstructural optimization and strengthening mechanisms of in-situ TiB_2/Al–Cu composite after multidirectional forging for six passes. *Int. J. Miner. Metall. Mater.* **2025**, *32*, 1703–1718. [CrossRef]
37. Zhang, J.; Kang, Z.; Zhou, L. Microstructure evolution and mechanical properties of Mg-Gd-Nd-Zn-Zr alloy processed by equal channel angular pressing. *Mater. Sci. Eng. A* **2015**, *647*, 184–190. [CrossRef]
38. Khan, F.; Panigrahi, S.K. Achieving excellent superplasticity in an ultrafine-grained QE22 alloy at both high strain rate and low-temperature regimes. *J. Alloys Compd.* **2018**, *747*, 71–82. [CrossRef]
39. Rokkala, U.; Bontha, S.; Ramesh, M.R.; Balla, V.K.; Srinivasan, A.; Kailas, S.V. Tailoring surface characteristics of bioabsorbable Mg-Zn-Dy alloy using friction stir processing for improved wettability and degradation behavior. *J. Mater. Res. Technol.* **2021**, *12*, 1530–1542. [CrossRef]
40. MD, F.K.; Karthik, G.M.; Panigrahi, S.K.; Janaki Ram, G.D. Friction stir processing of QE22 magnesium alloy to achieve ultrafine-grained microstructure with enhanced room temperature ductility and texture weakening. *Mater. Charact.* **2019**, *147*, 365–378. [CrossRef]
41. Xin, R.; Zheng, X.; Liu, Z.; Liu, D.; Qiu, R.; Li, Z.; Liu, Q. Microstructure and texture evolution of an Mg–Gd–Y–Nd–Zr alloy during friction stir processing. *J. Alloys Compd.* **2016**, *659*, 51–59. [CrossRef]
42. Rokkala, U.; Bontha, S. Influence of friction stir processing on microstructure, mechanical properties and corrosion behaviour of Mg-Zn-Dy alloy. *J. Mater. Sci.* **2023**, *58*, 2893–2914. [CrossRef]
43. Dong, B.; Che, X.; Zhang, Z.; Yu, J.; Meng, M. Microstructure evolution and microhardness of Mg-13Gd-4Y-2Zn-0.5Zr alloy via pre-solution and multi-directional forging (MDF) process. *J. Alloys Compd.* **2021**, *853*, 157066. [CrossRef]
44. Wang, Z.; Zhao, X.; Li, S.; Yu, J. Strengthening mechanism based on dislocation-twin interaction under room temperature multi-directional forging of AZ80 Mg alloy. *J. Mater. Res. Technol.* **2024**, *29*, 3656–3672. [CrossRef]
45. Wei, Q.; Yuan, L.; Ma, X.; Zheng, M.; Shan, D.; Guo, B. Strengthening of low-cost rare earth magnesium alloy Mg-7Gd-2Y–1Zn-0.5Zr through multi-directional forging. *Mater. Sci. Eng. A* **2022**, *831*, 142144. [CrossRef]
46. Wei, Q.; Yuan, L.; Shan, D.; Guo, B. Study on the microstructure and mechanical properties of ZK60 magnesium alloy with submicron twins and precipitates obtained by room temperature multi-directional forging. *J. Mater. Sci.* **2023**, *58*, 13236–13250. [CrossRef]
47. Khaleghi, A.A.; Salevati, M.A.; Sabbaghian, M.; Fekete-Horváth, K.; Drozdenko, D.; Máthis, K.; Akbaripanah, F. Comparing the microstructural and mechanical improvements of AZ80/SiC nanocomposite using DECLE and MDF processes. *Mater. Sci. Eng. A* **2024**, *892*, 146020. [CrossRef]
48. Li, J.; He, Z.; Fu, P.; Wu, Y.; Peng, L.; Ding, W. Heat treatment and mechanical properties of a high-strength cast Mg-Gd-Zn alloy. *Mater. Sci. Eng. A* **2016**, *651*, 745–752. [CrossRef]
49. Mohammed, S.M.A.K.; Chen, D.L.; Liu, Z.Y.; Ni, D.R.; Wang, Q.Z.; Xiao, B.L.; Ma, Z.Y. Deformation behavior and strengthening mechanisms in a CNT-reinforced bimodal-grained aluminum matrix nanocomposite. *Mater. Sci. Eng. A* **2021**, *817*, 141370. [CrossRef]
50. Praveen, T.R.; Shivananda Nayaka, H.; Swaroop, S.; Gopi, K.R. Strength enhancement of magnesium alloy through equal channel angular pressing and laser shock peening. *Appl. Surf. Sci.* **2020**, *512*, 145755. [CrossRef]
51. Song, G. The Effect of Texture on the Corrosion Behavior of AZ31 Mg Alloy. *JOM* **2012**, *64*, 671–679. [CrossRef]

52. Xin, R.; Luo, Y.; Zuo, A.; Gao, J.; Liu, Q. Texture effect on corrosion behavior of AZ31 Mg alloy in simulated physiological environment. *Mater. Lett.* **2012**, *72*, 1–4. [CrossRef]
53. Maric, M.; Muránsky, O.; Karatchevtseva, I.; Ungár, T.; Hester, J.; Studer, A.; Scales, N.; Ribárik, G.; Primig, S.; Hill, M.R. The effect of cold-rolling on the microstructure and corrosion behaviour of 316L alloy in FLiNaK molten salt. *Corros. Sci.* **2018**, *142*, 133–144. [CrossRef]
54. Cui, Q.; Yi, D.; Wang, H.; Zhang, J.; Xu, J.; Wang, B. Effects of grain size and secondary phase on corrosion behavior and electrochemical performance of Mg-3Al-5Pb-1Ga-Y sacrificial anode. *J. Rare Earths* **2019**, *37*, 1341–1350. [CrossRef]
55. Bahmani, A.; Lotfpour, M.; Taghizadeh, M.; Kim, W. Corrosion behavior of severely plastically deformed Mg and Mg alloys. *J. Magnes. Alloys* **2022**, *10*, 2607–2648. [CrossRef]
56. Zhang, Y.; Li, J.; Li, J. Microstructure, mechanical properties, corrosion behavior and film formation mechanism of Mg-Zn-Mn-xNd in Kokubo's solution. *J. Alloys Compd.* **2018**, *730*, 458–470. [CrossRef]
57. Zhou, Y.-L.; Li, Y.; Luo, D.-M.; Ding, Y.; Hodgson, P. Microstructures, mechanical and corrosion properties and biocompatibility of as extruded Mg–Mn–Zn–Nd alloys for biomedical applications. *Mater. Sci. Eng. C* **2015**, *49*, 93–100. [CrossRef]
58. Jana, A.; Balla, V.K.; Das, M. In-vitro corrosion and biocompatibility properties of heat treated Mg-4Y-2.25Nd-0.5Zr alloy. *Mater. Chem. Phys.* **2023**, *304*, 127873. [CrossRef]
59. Patel, V.; Li, W.; Andersson, J.; Li, N. Enhancing grain refinement and corrosion behavior in AZ31B magnesium alloy via stationary shoulder friction stir processing. *J. Mater. Res. Technol.* **2022**, *17*, 3150–3156. [CrossRef]

Disclaimer/Publisher's Note: The statements, opinions and data contained in all publications are solely those of the individual author(s) and contributor(s) and not of MDPI and/or the editor(s). MDPI and/or the editor(s) disclaim responsibility for any injury to people or property resulting from any ideas, methods, instructions or products referred to in the content.